Simultaneous reconstruction of scintillation light and ionization charge produced by 511 keV photons in liquid xenon : potential application to PET

P. Amaudruz[a], D. Bryman[*,b], L. Kurchaninov[a], P. Lu[b], C. Marshall[a], J. P. Martin[c], A. Muennich[a], F. Retiere[a], A. Sher[a]

[a]*TRIUMF, 4004 Wesbrook Mall, Vancouver, BC, V6T 2A3*
[b]*Department of Physics and Astronomy, University of British Columbia, 6224 Agricultural Road, Vancouver, BC, Canada V6T 1Z1*
[c]*University of Montreal, CP 6128 Succursale Centre-Ville, Montreal, Quebec, H3C 3J7 Canada*

Abstract

In order to assess the performance of liquid xenon detectors for use in positron emission tomography we studied the scintillation light and ionization charge produced by 511 keV photons in a small prototype detector. Scintillation light was detected with large area avalanche photodiodes while ionization electrons were collected on an anode instrumented with low noise electronics after drifting up to 3 cm. Operational conditions were studied as a function of the electric field. Energy resolutions of $< 10\%$ (FWHM) were achieved by combining the scintillation light and ionization charge signals. The relationship between scintillation light and ionization signals was investigated. An analysis of the sources of fluctuations was performed in order to optimize future detector designs.

Key words: Liquid Xenon, PET, Medical Imaging, TPC
PACS: 29.40.Gx, 87.57.-s, 87.57.uk

[*]corresponding author, Phone 001-604-222-7338, Fax 001-604-222-1074
Email addresses: amaudruz@triumf.ca (P. Amaudruz), bryman@phas.ubc.ca (D. Bryman), kurchan@triumf.ca (L. Kurchaninov), philipfl@phas.ubc.ca (P. Lu), cammarsh@triumf.ca (C. Marshall), jpmartin@lps.umontreal.ca (J. P. Martin), muennich@triumf.ca (A. Muennich), fretiere@triumf.ca (F. Retiere), sher@triumf.ca (A. Sher)

1. Introduction

Positron Emission Tomography (PET) is a functional imaging technique of growing importance in medical diagnostics. Its powers lie in the ability to reveal biologically significant processes that can be used, for example, in cancer screening and in studying neurodegenerative diseases. Conventional PET detectors employ scintillating inorganic crystals [1] as the gamma ray detection media. While crystal-based PET systems perform adequately for many applications there is motivation for seeking improvements of resolutions in energy, position, and time response to improve image quality and increasing overall sensitivity. Liquid xenon (LXe) is another gamma ray detector technology [2] applicable to high resolution PET which may result in improved performance and reduced noise in images due to superior energy resolution, true 3-dimensional position reconstruction, and the capability for determining the Compton scattering sequence [3, 4, 5]. Energy resolution of 7% (FWHM) has been reported in small LXe detector tests by combining scintillation light and ionization charge measurements [6]. Measuring charge in a drift chamber has been shown to provide 3-D sub-millimeter spatial resolution [7, 8] because electron diffusion is very small [9]. In addition, sub-ns timing resolution has been achieved by measuring the scintillation light [10]. Liquid xenon is also inexpensive compared to crystal detectors commonly used for PET. Liquid xenon PET systems have the potential to reduce detector contributions to PET to the level of intrinsic limitations due to positron range and non-colinearity of the emitted photons.

This paper deals with the energy resolution obtained from light and charge signals observed in a small LXe prototype detector as well as an investigation of the components influencing it and the sources of uncertainty which may inform the design of future detectors for PET.

2. Micro-PET Detector Design

We have developed a concept for a micro-PET detector shown in Fig. 1 that takes advantage of all the high resolution capabilities of LXe gamma ray detectors. Scintillation light is measured by arrays of large area avalanche photodiodes (LAAPD), which have been found to work well in LXe [11]. Charge measurement is achieved by using a time projection chamber (TPC), an approach successfully demonstrated in [7]. Photons entering the LXe produce prompt scintillation light and ionization which drifts under an electric field applied between the cathode and the anode of the TPC. The anode

module (not shown in Fig. 1) consists of a shielding grid followed by an array of wires preceding the anode which is segmented into strips perpendicular to the wires. The electron signal induced on the wires and collected by the strips provides a two dimensional (x-y) position measurement of the charge. The third coordinate (z) is obtained by measuring the electron drift time i.e. the difference between the time of the light flash and the electron arrival time on the anode. Since every interaction is precisely recorded, Compton scattering can be reconstructed giving information on the direction of each incoming photon providing the possibility to suppress accidental coincidences and scattering prior to reaching the detector.
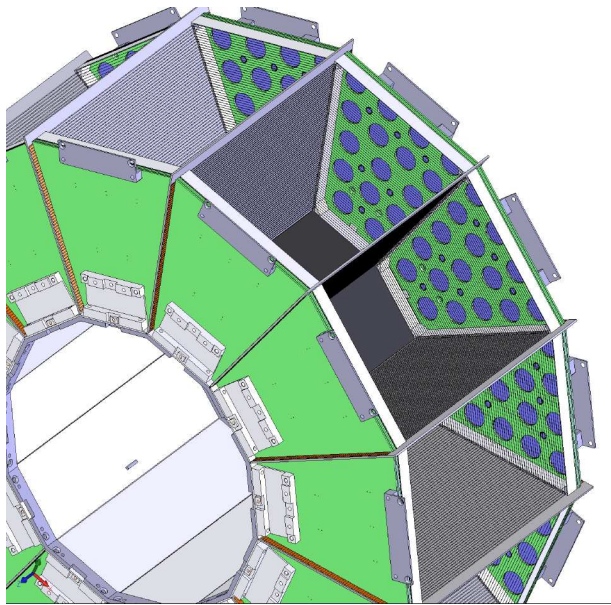

Figure 1: The LXe PET ring concept. Scintillation light and charge are measured in each of the 12 modules consisting of a LXe time projection chamber viewed by avalanche photodiodes.

The expectations for performance under operating conditions for PET include sub-millimeter 3-D position resolution from charge, timing resolution of < 1 ns from scintillation light, energy resolution $< 10\%$ (FWHM) combining light and charge signals, and the ability to reconstruct Compton scattering. Spatial location of events obtained from the prompt distributed light signals will be used to reduce the ambiguities of associating the scintillation light and charge at high levels of activity. A simulation of the imaging

₇₈ performance of this system will be presented in a future publication [12].

3. Small Chamber Prototype

3.1. Test Setup

₈₁ As an initial step in studying LXe detectors for PET, we constructed
₈₂ a small test chamber (27 cm^3) for simultaneous measurements of light and
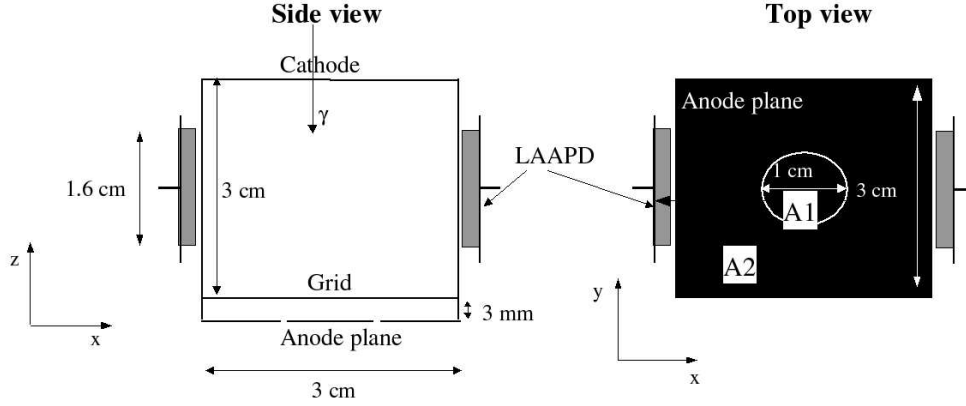₈₃ charge. The test chamber is shown schematically in Fig. 2.

Figure 2: Schematic views of the small test chamber. The side view illustrates the drift direction between the cathode and anode, viewed by two LAAPDs immersed in the LXe. The top view shows the segmentation of the anode.

₈₄ Scintillation light was detected by two 1.6 cm diameter windowless
₈₅ LAAPDs (Advanced Photonics Inc. [16]). The LAAPDs were located at
₈₆ the center of the drift region as shown in Fig. 2, 1.5 cm above the grid wires
₈₇ and 1.5 cm below the cathode. Charge was collected on a central 1 cm di-
₈₈ ameter electrode (A1) or on an outer electrode (A2). An electric drift field
₈₉ was applied between the cathode and a shielding grid separated by 3 cm.
₉₀ The electric field was formed by a field cage consisting of 9 wires with a
₉₁ spacing of 3 mm strung along the four walls of the chamber. The voltage
₉₂ was distibuted by 100MΩ resistors. The APDs were outside the field cage
₉₃ and the distance between the field cage wires and the APDs was 2mm. The
₉₄ shielding grid consisted of 0.1 mm dia. wires spaced by 3 mm located 3 mm
₉₅ from the anode charge collection plane. The electric field between the grid
₉₆ wires and the anode was set higher than the drift field ensuring that all

the electrons pass through the grid [13]. In order to study the influence of the drift field on quantities like charge and light production and the energy resolution several settings were used. With the grid at ground potential measurements were made with the negative cathode voltage set to 1, 3, 6, and 8 kV, with the respective anode voltages set to 300, 600, 1200 and 1200 V. Photons of 511 keV emitted after annihilation of positrons from a ^{22}Na source with an activity of $9.61 \cdot 10^5$ Bq and situated in a collimator with an opening angle of $2°$ positioned 30 cm away from the cathode entered the test chamber (along the z axis) through the cathode plane. The trigger was generated by selecting signals in coincidence of both APDs and an external NaI detector placed at a distance of 50 cm from the source observing the full energy of the other 511 keV photon from the positron annihilation. The probability to detect more than one event in the chamber at the same time was less than 3%. The detector was operated at 15 psia and at temperatures between 168 and 169 K. Before inserting the liquid in the vessel holding the detector a bake-out in vaccuum at $7.6 \cdot 10^{-6}$T was performed for 6 days at $60°$C to clean the components. The purification of the xenon was done in the gas phase using two stages both with equipment from From NuPure Corporation [14]: first, the heated getter (NuPure Omni 600) was used to remove $H_2 0$, O_2, CO, H_2, and N_2 to sub-ppb levels followed by a room temperature getter (Eliminator 600 cg) to remove $H_2 0$, O_2, CO, H_2, and hydrocarbons to < 0.5 ppb. The lifetime of drifting ionization electrons was used to indicate successful operation of the purification as discussed below.

3.2. Readout Electronics

The two anodes segments and the grid wires (ganged together) were connected to charge-sensitive amplifiers followed by a 1 µs time constant RC-CR shaper. The amplifier was calibrated using a narrow pulse input charge with a precision of 5%. The amplifier outputs were fanned out into three branches:

1. A constant fraction discriminator followed by a time-to-digital converter (TDC) CAEN model V1190B;
2. A charge sensitive analog-to-digital converter: 12 bit QDC CAEN model V792 with gate adjusted to the drift time and pulse shape; and
3. A 20 MHz sampling waveform digitizer VF48 [15].

To get absolute charge values, the digitized waveform measured with the VF48 was used for the analysis presented in sections 4 and 5. Because the

QDC had a better signal to noise ratio it was used to determine the energy resolution in section 6 which did not require absolute charge calibration. The other reason the QDC was not used for absolute values was due to the very short pulse used for calibration. The longer chamber signal would not have been fully integrated within the window set.

The observed range of noise of the amplifier was 700-1100 electrons due to varying external sources of induced noise. To reach the optimal position resolution, a signal to noise ratio larger than 5 was desirable requiring the electronics noise to be kept below 1000 electrons equivalent noise charge (ENC). A typical signal was expected to be at least 10 000 e-, as long as the electron attachment during the drift was small.

The LAAPD voltages were set so that their gains were 500 and each was connected to a current-sensitive preamplifier with a pulse width of 50 ns and 10^4 electrons ENC. The amplifier signal was split into 3 branches:

1. Discriminator and TDC;
2. QDC CAEN model V792 with a gate of 100 ns; and
3. 1 GHz waveform digitizer CAEN model V1729.

Solid angle calculations showed that 12% of the scintillation photons reached the LAAPDs when the gamma interaction took place in the center of the chamber.

4. Charge Collection

The grid wires shielded the anodes from the current induced by the drifting electrons. Once the ionization electrons passed the grid wires the signal on the anode started to build up with a pulse shape that was largely independent of the z position of the primary interaction although electrostatic calculations showed that the current pulse shape depended on the x-y distance of the electron cloud from the individual grid wires. Furthermore, depending on the drift velocity (typically 0.15 to 0.21 cm/µs), the current induced on the anodes lasted 1.5 to 2 µs.

The waveforms measured on the grid and on the two anodes provided information about the location of charge creation and Compton scattering if multiple charge pulses were observed. The time of charge arrival relative to the light signal gave information about the position along the drift direction of the electrons.

Figure 3 shows examples of four charge waveform events recorded by the 20 MHz waveform digitizers chosen to illustrate several types of events.
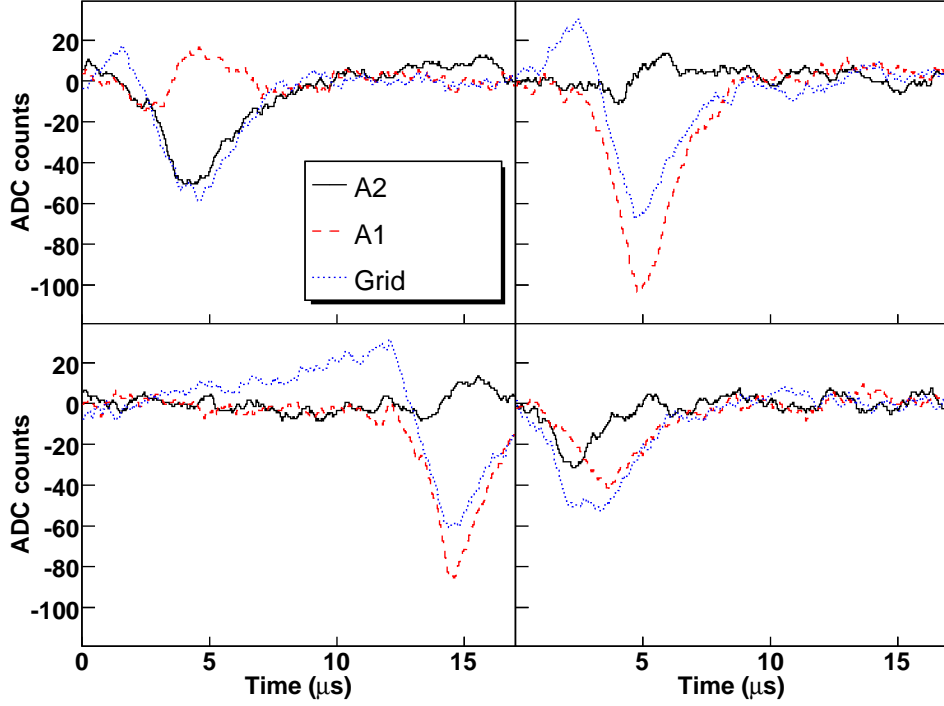
Figure 3: Example of waveforms with a 2 kV/cm drift field. Central anode A1 (dashed line), peripheral anode A2 (solid line), grid (dotted line).

In the upper two plots the charge was created roughly at the same z position; in the left plot the signal of the central anode (A1) integrated to zero and the anode A2 collected the charge, whereas in the right hand plot the interaction deposited the full charge on the central anode A1. The lower left panel shows an event originating close to the cathode plane, resulting in a measured drift time of 15 µs. The charge was collected by the central anode. The bipolar shape of the grid signal is clearly visible. The waveform measured on the grid depends on the z position of the interaction and is also influenced by electrons collected by the grid. The lower right panel shows two photon interactions, presumably one Compton scattering and one photo-electric interaction. One interaction took place above A1 and one above A2. The interactions were also separated in the drift direction so that a two peak structure is visible in the grid waveform. Simulations of the setup showed that only a small fraction (less than 5%) of events fully con-

tained on A1 have mutliple hits that can be detected. The total charge for these events however is not significantly different from the events with just one interaction. For this analysis we did not treat them separately since we were primarily interested in the total charge deposited on the anode. Better separation of multiple photon interactions on an event by event basis will be possible with finer segmentation of the readout electrodes and shorter shaping time.

The purity of the LXe has an impact on charge collection. In the current setup we achieved an electron lifetime of 200 μs using purification in the gas phase with heated getters[1]. We estimated that the level of purity obtained would result in a loss of 8% of the electrons due to attachment.

For the analysis in this paper we selected events where no net charge was measured on A2. By demanding the absence of charge on A2 the region of A1 in which events were accepted was smaller than its physical size since charge depositions close to the edge of A1 induced charge on A2. The effective radius of the tube in which events were accepted was estimated to be 0.45 cm compared to the A1 radius of 0.5 cm.

Figure 4 shows the distribution of charge due to 511 keV photons incident on the chamber as measured on A1 as a function of the drift time for a 1 kV/cm drift field. The shape of the distribution is the same for all drift fields. The 511 keV band rises sharply in less than 1 μs, and then falls slowly until the cutoff which corresponds to the edge of the chamber. The sharp rise corresponds to photons interacting between the grid and anode. In that case the electronics, which is not sensitive to the charge induced by the much slower drifting ions, measures only a fraction of the charge which is approximately proportional to the distance between the anode and the interaction point. When the interaction point is between the grid and the cathode, the measured charge should be independent of the interaction position. The decline of measured charge with increasing drift times is due to electron attachment by impurities in the LXe.

Compton scattering interactions are evident below the 511 keV band. They are due to photons entering the chamber with less than 511 keV because they have scattered in the passive detector material, mostly the 2 cm of LXe between the vessel wall and the cathode, and to photons escaping after a Compton scattering interaction in the liquid.

---

[1] A problem occurred with the purification system during the data taking with the NaI coincidence trigger used in this paper resulting in an electron lifetime of 90 μs for much of the data presented here.
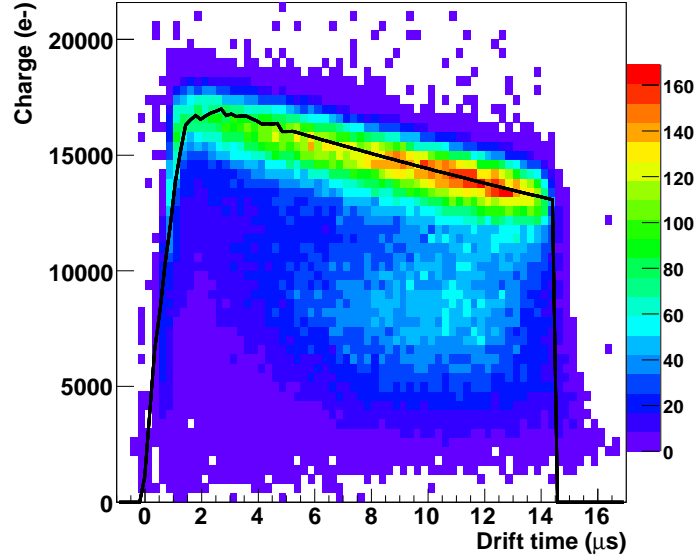
Figure 4: Charge collection as a function of drift time for a 1 kV/cm drift field. The curve is a fit based on parametrization obtained from current calculations for energy deposits of 511 keV. The scale on the right corresponds to the number of events that occurred at a specific time with a certain charge deposition.

We performed a fit of the 511 keV band to extract the drift velocity v_d, the total charge Q_{tot} produced in the photon interaction and the attenuation length. The values obtained for these quantities are listed in Table 1 with their statistical uncertainties from the fits. The charge yield Q_{tot}/Q_0 is also shown along with Q_{tot} which is the measured charge corrected for attachment and electronics calibration and Q_0 is the ratio of the energy deposited by the γ-ray and the average energy to produce an electron ion pair: $Q_0 = E_\gamma/W$ with W=15.6 eV [17].

Figure 5 shows the comparison of our results for the charge yield to the values obtained in [6] and [18]. Our results lie in between the two previous measurements of the charge yield. The obtained drift velocity was in agreement with previous measurements in [19].

E_d [kV/cm]	v_d [cm/µs]	Q_{tot} (511 keV e$^-$)	τ [µs]	$\frac{Q_{tot}}{Q_0}$
0.33	0.16 ± 0.01	$19\ 707 \pm 55$	94 ± 3	0.60
1	0.18 ± 0.01	$23\ 372 \pm 59$	61 ± 2	0.71
2	0.20 ± 0.01	$25\ 092 \pm 100$	76 ± 5	0.77
2.66	0.20 ± 0.01	$24\ 761 \pm 35$	60 ± 1	0.76

Table 1: Drift velocity (v_d),number of electrons (Q_{tot}), electron lifetime τ and charge yield observed for different electric fields (E_d).
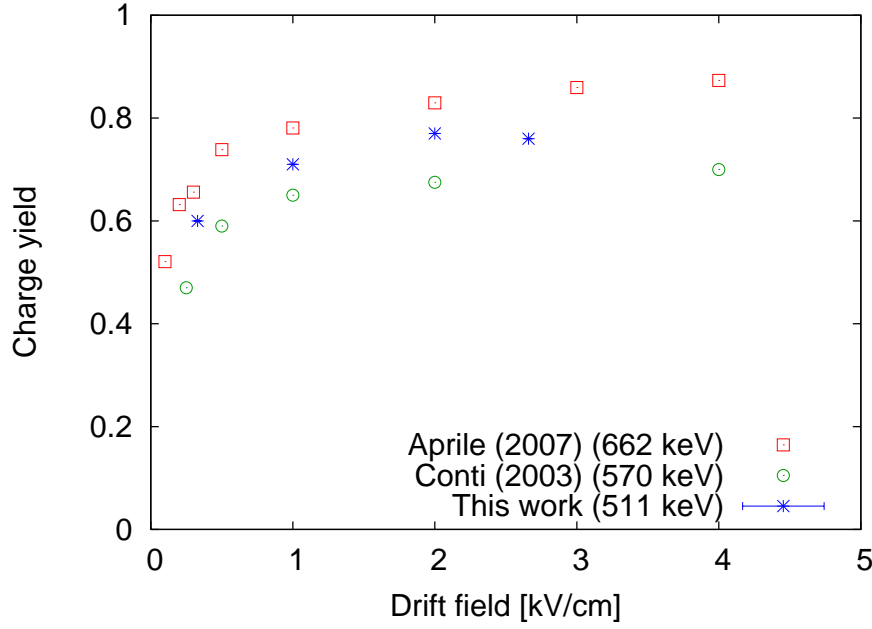

Figure 5: Charge yield measured by different groups at different γ-ray energies: this work marked with $\star$, [6] with $\square$ and [18] with $\bigcirc$.

5. Light Collection

Scintillation light was detected by the LAAPDs located on two sides of the chamber. Figure 6 shows the sum of the number of photons measured by both LAAPDs as a function of the electron drift time for the events where all the charge was collected on the central anode.

The bell shape in Fig. 6 is due to variations of the solid angle with drift distance which can be calculated by integrating over the LAAPD area for a given location in the chamber assuming no reflections occurred in
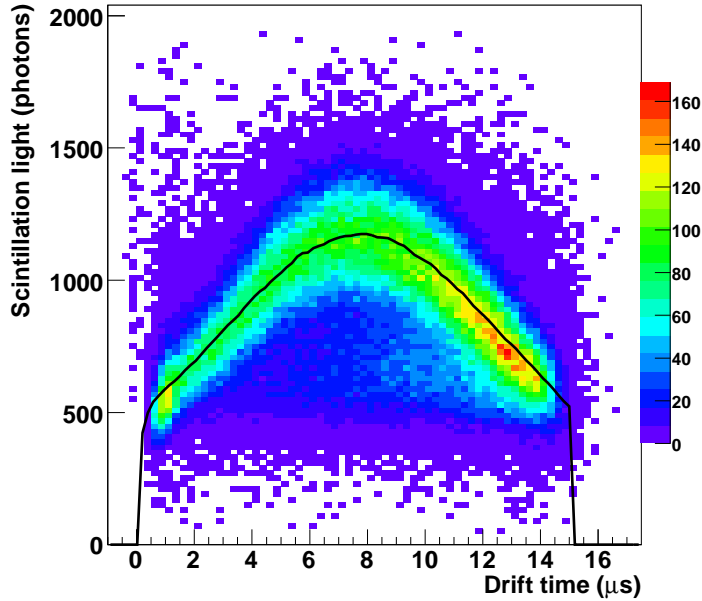
Figure 6: Light collection as a function of drift time for a 1 kV/cm drift field at 511 keV. The curve is a fit based on parametrization obtained from solid angle calculations. The scale on the right corresponds to the number of events that occurred at a specific time with a certain charge deposition.

the chamber walls. The solid angle varied significantly with the position of the photon interaction. The arrival time of the electrons provided a handle on the solid angle variation in the drift direction. However, there was no information about the position of the interaction within the disk defined by A1. When the LAAPDs were used independently, the solid angle variation within this disk introduced a 22% fluctuation in the light collection. Combining both LAAPDs reduced the fluctuation to 6%.

We fitted the distribution in fig. 6 using a parametrization of the solid angle, with the total number of photons and the drift velocity as free parameters. The fit parameters are shown in Table 2. The drift velocity is consistent with the one extracted from the fit to the charge distribution. The total number of photons drops with increasing drift voltage in agreement with previous measurements [6, 18]. The number of photons actually created within the detector was not extracted in this analysis because we did not measure the photon detection efficiency (PDE) of the LAAPDs. One of the LAAPDs detected more photons than the other one, which sug-

gests that there may be a variation of the PDE between LAAPDs[2]. In the results given in Table 2, we have assumed 100% PDE for the LAAPD that exhibited a more stable operation and scaled the light measured by the other LAAPD accordingly introducing a systematic uncertainty because of the unknown efficiency (which may be up to 50%). Uncertainties also originated from the fact that the ratio between the mean value measured by the two LAAPDs varied between data sets by 10%. The light yield was computed using a value of 13.8 eV [17] needed to create one photon at zero drift field resulting in $S_0 = 37029$ photons. N_{tot} is the number of measured photons corrected for the solid angle of the geometry but not corrected for the photo detection efficiency of the LAAPDs.

E_d [kV/cm]	v_d [cm/µs]	N_{tot} (511 keV e$^-$)	N_{tot}/S_0
0.33	0.15 ± 0.01	$12\ 161 \pm 1269$	0.33
1	0.18 ± 0.01	$10\ 113 \pm 1055$	0.27
2	0.20 ± 0.01	9243 ± 964	0.25
2.66	0.21 ± 0.01	7936 ± 828	0.21

Table 2: Electric field (E_d), drift velocity (v_d), number of photons (N_{tot}) and light yield observed (see text) for 511 keV photon interactions.

Figure 7 shows the comparison of our results with values obtained in [6] and [18]. If the quantum efficiency of the LAAPDs was 60%, which later results presented here suggest, our results would be in agreement with previous measurements.

6. Light and Charge Combination

To study the energy resolution we focused on the central region of the chamber by selecting events with no charge on A2 and choosing a time window in the drift direction corresponding to 2 mm drift located on the axis of the LAAPDs where the light collection is maximal as shown in Fig. 6. The charge signals were corrected for attenuation and the light signals for the difference between the two LAAPDs and the solid angle dependence in the drift direction. Resolution results are given as the standard deviation (σ) of a Gaussian distribution unless otherwise stated. Figure 8 shows

---

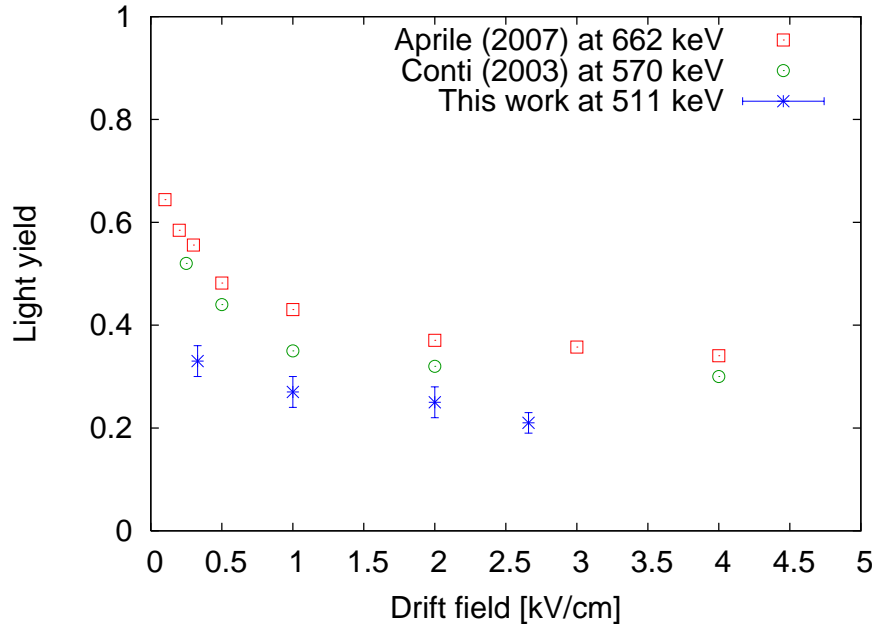[2]This may explain the apparent discrepancy between measurements made by different groups [21]

Figure 7: Light yield relative to the maximum yield measured by different groups at different γ-ray energies: this work marked with $\star$, [6] with $\square$ and [18] with $\bigcirc$.

the analysis of a data run at a drift field of 2.66 kV/cm. Evaluating the charge and light signals separately gave energy resolutions of 12.1% for light and 5.4% for charge by fitting the spectra (shown in the upper plots of Fig. 8) with a sum of two Gaussians and evaluating the mean and width of the 511 keV peak. The energy resolution can be improved significantly by combining the information from light and charge using the anti-correlation of the two signals [6, 18, 20]. The lower left plot of Fig. 8 shows the linear anti-correlation between the light and charge measurement and the axis of the ellipse. Selecting the 511 keV region of the photo-electric-peak the correlation angle was obtained from a linear fit which provided the axis of the charge-light ellipse. Projecting the data points along this axis as described in [6] gave the overall energy resolution. The correlation angle given here depended on the detector geometry and the efficiency to measure light and charge separately. The upper left plot shows the charge spectrum collected on the anode which is equal to a projection of the correlation along the light axis. In the upper right plot the projection of the correlation along the charge axis can be seen, giving the spectrum of the collected

light. The lower right plot demonstrates the improved energy resolution of the combined spectrum when projecting along the correlation axis and normalizing to the mean charge. The sum of three Gaussians was used as the fit function to account for the three contributions to the spectrum: the Compton region (C), the photoelectric peak (P), and scattered events (S) which lost energy outside the detector, mostly in the LXe before entering the chamber.
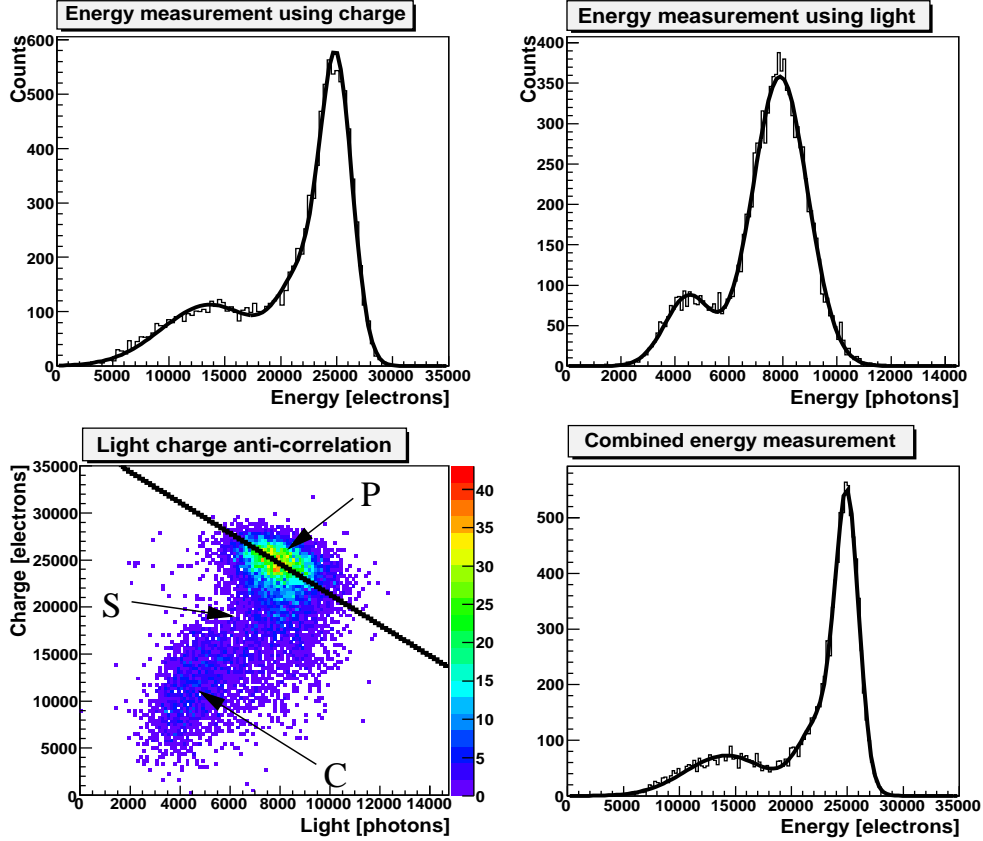

Figure 8: The observed charge spectrum (upper left plot), light spectrum (upper right plot), correlation between light and charge signals (lower left plot), and combined spectrum using the correlation (lower right plot) for 511 keV photons with a drift field of 2.66 kV/cm. The data points in the correlation plot (lower left) that are not part of the Compton (C) or the photoelectric peak (P) are due to photons that scattered outside the detector (S). The linear fit (solid line) giving the axis of the correlation ellipse is depicted as well. The fits shown (solid lines) were made with a sum of 3 Gaussians (upper left and lower right plot) or 2 Gaussians (upper right plot).

Another variable to quantify the anti-correlation between light and charge is the correlation coefficient ρ [22]. Assuming that the probability for a recombining electron-ion pair to produce a scintillation photon is 1 and the detector would be able to measure light and charge with 100% efficiency and perfect resolution, ρ should be -1. Deviation from -1 could be due to other sources of fluctuations like density fluctuations or delta electrons as discussed in [23] and the references within.

Table 3 gives the results of the analysis for different drift fields. The best combined energy resolution reached for these data sets was 4.1% at 2.66 kV/cm drift field (see below).

E_d	Energy resolution [%]			θ_{corr}	ρ
[kV/cm]	light	charge	combined	[°]	
0.33	13.5 ± 0.2	7.3 ± 0.5	4.7 ± 0.1	56	-0.46
1	12.2 ± 0.2	6.0 ± 0.3	4.3 ± 0.3	59	-0.34
2	12.8 ± 0.5	7.0 ± 0.6	4.8 ± 0.4	62	-0.34
2.66	12.1 ± 0.1	5.4 ± 0.2	4.1 ± 0.1	58	-0.26

Table 3: Energy resolutions (σ) observed at different drift fields for light and charge separately and combined result using the correlation.

7. Discussion of Error Sources

In this section we discuss contributions to the energy resolution that were due to detector inefficiencies or physics constraints like light-charge-fluctuations. When a photon interacts there is an initially produced number of ionization charges and scintillation photons which is modified by recombination dependent on the presence of an applied electric field. Table 4 summarizes the variables used in the calculation of error contributions.

	Charge	Scintillation light
Initial	Q_i	S_i
Final	$Q_f = Q_i[1 - F_r(E_d)]$	$S_f = S_i + Q_i F_r(E_d) P_{e \to h\nu}$
Measured	$Q_m = A \, Q_f$	$S_m = F_\Omega \epsilon S_f$

Table 4: Parameters used in the discussion of energy resolution as described in the text.

Q_i, Q_f and Q_m (S_i, S_f and S_m) are the numbers of initially produced, post-recombination, and measured charge (light) signals respectively. $F_r(E_d)$

is the fraction of electron-ion pairs that recombine for a given electric field E_d, and $P_{e \to h\nu} = 1$ [6] gives the probability for a recombining electron-ion pair to produce a scintillation photon. Impurities may capture some electrons, which is accounted for by an attenuation parameter A, which depends on the electron drift distance. The photo-detectors have a photo-detection efficiency ϵ and cover a fraction of the total solid angle F_Ω.

7.1. Charge

The charge resolution is dominated by electronics noise and charge-light fluctuation. The charge-light fluctuation is expressed by the fluctuation of the recombination fraction F_r, ΔF_r. The charge resolution can then be written as

$$\left(\frac{\Delta Q_m}{Q_m}\right)^2 = \left(\frac{ENC_q}{Q_m}\right)^2 + \left(\frac{\Delta F_r}{1 - F_r}\right)^2 + \frac{1 - A}{Q_m} \tag{1}$$

where the first term on the right describes the electronics noise of the amplifier, the second term quantifies the light-charge fluctuation, and the third contribution is the attachment factor which is negligible. ΔF_r describes the fluctuation of the recombination and will also occur in the discussion of the error sources for the light measurement in the next section. Table 5 gives values for the error contributions to the energy resolution obtained from the charge measurement. Also shown is the intrinsic energy resolution found by subtracting the noise of the electronics from the measured resolution. The only unknown variable contributing to the error of the energy resolution is ΔF_r which can be calculated once the intrinsic energy resolution is known. The values for ΔF_r obtained can also be found in Table 5.

E_d [kV/cm]	Measured res. [%]	Noise [%]	Intrinsic res. [%]	ΔF_r [%]
0.33	7.31 ± 0.54	5.03 ± 0.04	5.3 ± 1.5	3.2 ± 0.9
1	6.04 ± 0.33	4.22 ± 0.03	4.3 ± 0.9	3.1 ± 0.7
2	7.00 ± 0.62	4.29 ± 0.03	5.5 ± 1.6	4.2 ± 1.2
2.66	5.43 ± 0.17	3.48 ± 0.03	4.2 ± 0.4	3.2 ± 0.3

Table 5: Contribution of error sources to the energy resolution obtained from the charge measurement.

7.2. Light

The fluctuations in the LAAPD specified as the excess noise factor $F(M) = 2 + kM$ is dependent on the gain M and affects the resolution. For this setup with $k = 0.001$, $F(M) = 2.5$. Furthermore, the LAAPD gain $< 10^3$ requires that low noise electronics must be used to further amplify the signal, which adds electronic noise ENC_s. Another source of fluctuations arises because the solid angle seen by the photo-sensor may vary on an event-by-event basis since the solid angle changes with the position of the photon interaction within A1. This fluctuation can be corrected for if the interaction position is known well from the ionization signal.

Neglecting other detection fluctuations, the light signal resolution for our setup can be written as:

$$
\begin{aligned}
\left(\frac{\Delta S_m}{S_m}\right)^2 &= \left(\frac{ENC_s}{MS_m}\right)^2 + \frac{F(M)}{S_m} \\
&+ \left(\frac{\Delta F_\Omega}{F_\Omega}\right)^2 + \left(\frac{P_{e\to h\nu}Q_i\Delta F_r}{S_f}\right)^2 \\
&+ \frac{F_r Q_i P_{e\to h\nu}(1 - P_{e\to h\nu})}{S_f^2}
\end{aligned}
\tag{2}
$$

where the first term on the right represents the electronics noise, the second term gives the contribution from fluctuations in the LAAPD gain, the third term is the fluctuation of the solid angle due to the position of the light creation inside the chamber and the fourth term describes the light-charge fluctuation. The contribution of the fluctuation in $P_{e\to h\nu}$ given by the last term is negligible or exactly zero if $P_{e\to h\nu} = 1$. Table 6 gives values for the error contributions to the measured energy resolution from the scintillation light. The solid angle fluctuation amounted to 5.6% and was independent of the drift field. Also shown is the intrinsic energy resolution found when subtracting those error sources due to the detector from the measured resolution. ΔF_r was calculated again and can be compared to the values obtained from the charge measurement. The values for ΔF_r from both the light and charge measurements are in good agreement within statistical errors providing a consistency check for the error analysis.

7.3. Combination

Combining the light and charge allows improvement to the resolution by canceling the fluctuations of F_r by making use of the anti-correlation,

E_d [kV/cm]	Measured res. [%]	Noise [%]	LAAPD fluct. [%]	Intrinsic res. [%]	ΔF_r [%]
0.33	13.5 ± 0.2	3.3	0.46	9.6 ± 0.4	5.8 ± 1.3
1	12.2 ± 0.2	4.0	0.55	6.8 ± 0.8	3.3 ± 1.0
2	12.8 ± 0.5	5.1	0.56	7.1 ± 1.7	3.1 ± 1.2
2.6	12.1 ± 0.1	4.7	0.63	5.5 ± 0.5	2.5 ± 0.8

Table 6: Contribution of error sources to the energy resolution obtained using the light measurement.

provided the measured charge is corrected for attenuation and the measured light for solid angle and PDE:

$$E_c = \frac{Q_m}{A} + \frac{S_m}{F_\Omega \epsilon} \tag{3a}$$

$$= Q_f + \frac{S_f}{P_{e \to h\nu}} \tag{3b}$$

$$= Q_i (1 - F_r) + \frac{S_i}{P_{e \to h\nu}} + Q_i F_r \tag{3c}$$

$$= Q_i + \frac{S_i}{P_{e \to h\nu}} \tag{3d}$$

where E_c is the energy measured by combining the charge and light signals: In eq. 3a the light and charge signals were combined; eq. 3b and eq. 3c made use of the formulas in Table 4; and in eq. 3d F_r was eliminated. The remaining uncertainty in the combined energy resolution is then:

$$\Delta E_c^2 = \frac{1}{\epsilon^2 F_\Omega^2} \left[\left(\frac{ENC_s}{M} \right)^2 + F(M) S_m + \left(\frac{\Delta F_\Omega S_m}{F_\Omega} \right)^2 \right]$$
$$+ \left(\frac{ENC_q}{A} \right)^2 \tag{4}$$
$$+ \frac{Q_f(1 - A)}{A} + \frac{F_r Q_i(1 - P_{e \to h\nu})}{P_{e \to h\nu}}$$

where the first term on the right hand side (in brackets) originated from the light signal contribution and the second term from the charge measurement. The last two terms describing the contributions from the binomial statistics of A and $P_{e \to h\nu}$ are negligible.

Table 7 gives the calculated values for the combined energy resolution $\Delta E_c/E_c$. The intrinsic combined energy resolution given in the last column of table 7 was obtained by subtracting $\Delta E_c/E_c$ in quadrature from the measured values. The solid angle was 12% and the efficiency ϵ for the LAAPDs was assumed to be 1.

E_d [kV/cm]	Meas. comb. res [%]	$\Delta E_c/E_c$ [%]	Intr. comb. res. [%]
0.33	4.74 ± 0.09	4.0 ± 0.1	2.5 ± 0.4
1	4.31 ± 0.26	3.7 ± 0.1	2.3 ± 1.0
2	4.78 ± 0.35	3.8 ± 0.1	2.9 ± 1.2
2.66	4.14 ± 0.10	3.3 ± 0.1	2.5 ± 0.4

Table 7: Contribution of error sources and corrected intrinsic energy resolution for combined charge-light measurement.

The intrinsic correlation coefficient was calculated but showed a large uncertainty due to the impact of the uncertainty on ΔF_r.

Another consistency check of the formulas presented here can be made by extracting the factor $\epsilon P_{e \rightarrow h\nu}$ in two different ways from the data. We cannot disentangle the efficiency from the probability but the product can be obtained from the correlation angle of the 511 keV cloud by writing Q_m/A as a function of S_m/F_Ω with the slope m describing the axis of the ellipse:

$$\frac{Q_m}{A} = Q_f = m\frac{S_m}{F_\Omega} + const. \tag{5}$$

$$\Longrightarrow \theta_{corr} = \arctan\left(\frac{-1}{\epsilon P_{e \rightarrow h\nu}}\right)$$

The results are listed in Table 8. The mean value over all runs was $\epsilon P_{e \rightarrow h\nu} = 0.60 \pm 0.03$.

The other method for extracting $\epsilon P_{e \rightarrow h\nu}$ is to find the slope from the plot of the mean values of light vs. charge (coordinates of the center of the ellipse) for each electric field setting. This is shown in Fig. 9. The linear fit to this data gave a slope of $\epsilon P_{e \rightarrow h\nu} = 0.7 \pm 0.3$ which agrees with the value obtained from the event-by-event method. This result would be consistent with $P_{e \rightarrow h\nu} = 1$ if the efficiency of the APDs were 60%.

E_d [kV/cm]	θ_{corr}	$\epsilon P_{e \to h\nu}$
0.33	56.2	0.67 ± 0.03
1	58.7	0.61 ± 0.11
2	62.3	0.53 ± 0.30
2.66	58.5	0.61 ± 0.05

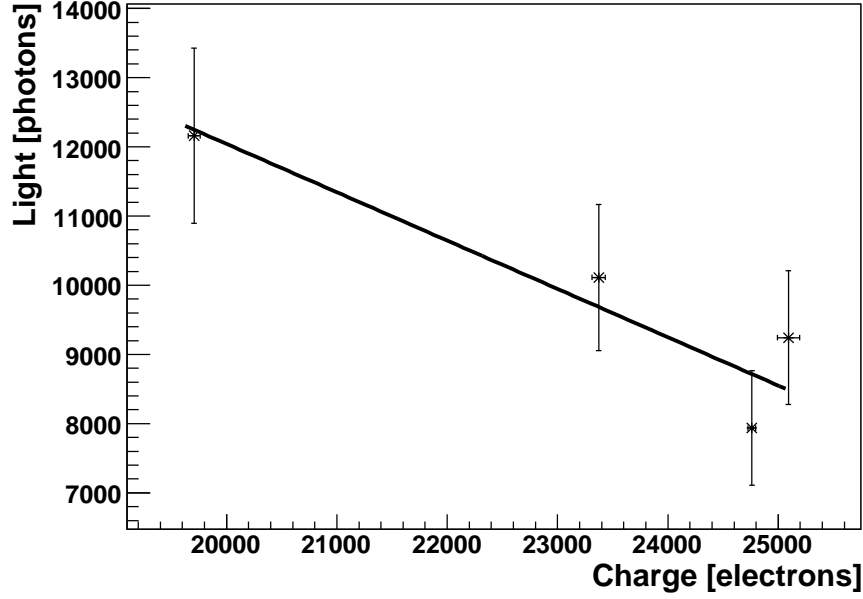Table 8: Calculating $\epsilon P_{e \to h\nu}$ on event by event basis.

Figure 9: Method of extracting $\epsilon P_{e \to h\nu}$ from mean values of the correlation cloud parameters described in the text. The solid line is the linear fit to the data.

7.4. Improving Light Resolution using Position Reconstruction

In the current system, the energy resolution contribution from light was partially limited by the uncertainty in the position of the light source due to the 1 cm dia. size of A1 i.e. from the fluctuation of the solid angle within A1. Applying the formulas presented above to a Geant4 [24] simulation, it was found that knowing the position of the light signal to 1 mm would improve the light resolution by about 1.5% and the combined resolution by up to 0.5% giving 10% for light alone and 3.6% for the combination of charge and light, consistent with the resolution reported in [6]. Table 9 summarizes the

values obtained with the simulation comparing the two cases of not knowing the position of the interaction within A1 and being able to correct for it.

	Light res. [%]	Charge res. [%]	Combined res. [%]
Measured	12.1 ± 0.1	5.4 ± 0.2	4.1 ± 0.1
Simulated	12.0 ± 0.2	5.4 ± 0.1	3.9 ± 0.1
Corrected	10.4 ± 0.2	5.4 ± 0.1	3.6 ± 0.1

Table 9: Energy resolutions obtained from the simulation with (corrected) and without (simulated) the correction for the position of the interaction within A1 in comparison with the measured resolutions. The charge resolution was not affected by the correction.

8. Summary and Conclusion

Measurements have been made of the response of a liquid xenon drift chamber to irradiation by 511 keV photons. Using a model accounting for the sources of uncertainty in the energy resolution we also determined values for the intrinsic energy resolutions. Figure 10 summarizes the results for charge, light and combined energy resolution as a function of the drift field. The main error contribution to the combined energy resolution, apart from the solid angle fluctuations which can be eliminated by utilizing the position measurement, originated from the APD gain fluctuation and the anode noise. Both were about of 2.7%.

Figure 11 depicts the values for the intrinsic energy resolutions obtained by subtracting the detector contributions from the values in fig. 10. The error bars given are statistical.

Based on these results, the combined energy resolution of <3.5% (or < 8% FWHM) would be anticipated in a detector configuration suitable for applications to PET which would have comparable light collection efficiency to the prototype detector described above and <1 mm spatial resolution. Reducing the anode to grid spacing to 1 mm and the grid wire spacing to 1 mm will reduce the width of the pulses and minimize the dependence of the pulse shape on the location of the electron cloud. Further improvements are foreseen in areas including purification and low noise electronics.

Acknowledgments
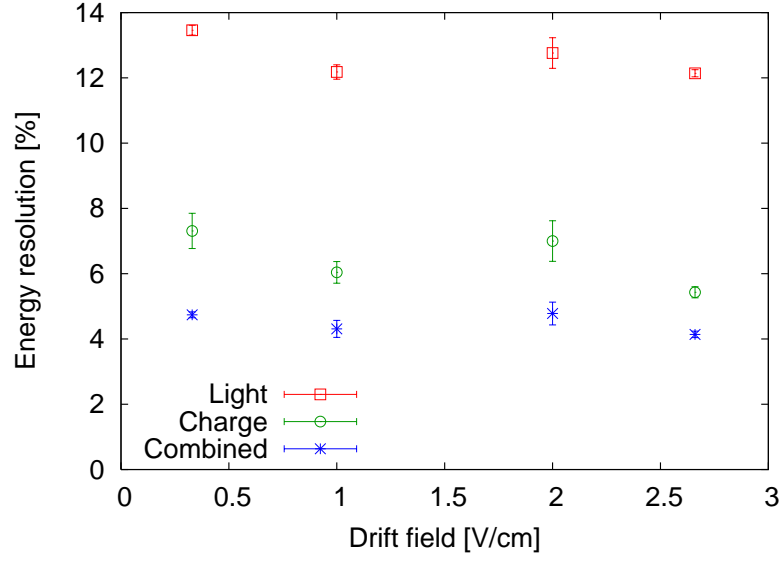
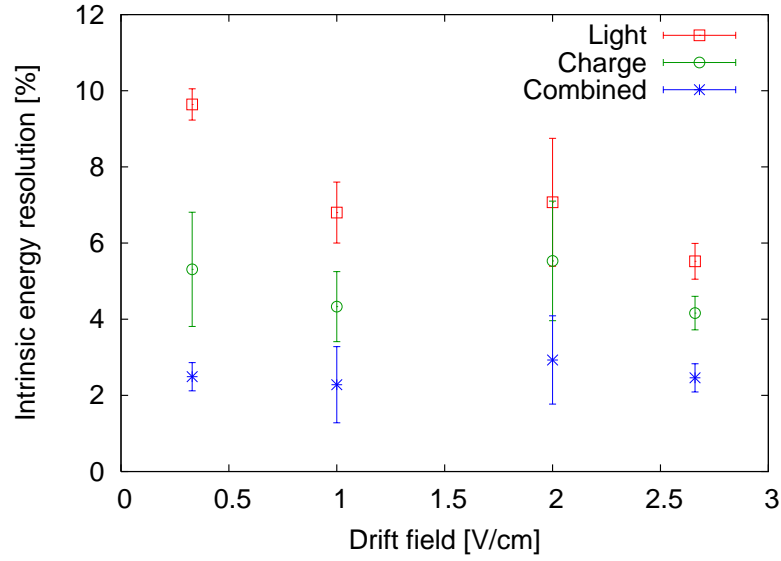Figure 10: Energy resolution from charge (○) and light (□) measurements as well as the combined (⋆) resolution for different drift fields.

Figure 11: Intrinsic energy resolution from charge (○) and light (□) measurements as well as the combined (⋆) intrinsic resolution for different drift fields.

References

[1] See , for example, Jin Su Kim *et al.*, *Performance Measurement of the microPET Focus 120 Scanner*, The Journal of Nuclear Medicine, Vol. **48** (2007), No. 9, p. 1527.

[2] E. Aprile *et al.*, *Noble Gas Detectors*, Wiley-VCH, Berlin, 2006, ISBN-10: 3-527-40597-6.

[3] K. Giboni *et al.*, *Compton Positron Emission Tomography with a Liquid Xenon Time Projection Chamber*, JINST **2** (2007) P10001.

[4] Chepel, V.Y., *A new liquid xenon scintillation detector for positron emission tomograph*, Nucl. Tracks Radiat. Meas **21** (1993), pp. 47.

[5] M.I.Lopes *et al.*, *Performance analysis based on a Monte-Carlo simulation of a liquid xenon PET detector*, IEEE Trans. Nucl. Sci. NS-42, No**6** (1995),pp. 2298-2302.

[6] E. Aprile *et al.*, *Observation of Anti-correlation between Scintillation and Ionization for MeV Gamma-rays in Liquid xenon*, Phys. Rev. B **76** (2007), 014115.

[7] E. Aprile *et al.*, *Compton Imaging of MeV Gamma-Rays with the Liquid xenon Gamma-Ray Imaging Telescope (LXeGRIT)*, submitted to Nucl. Instr. and Meth. A , Vol. **593** (2008), p. 414-425.

[8] V.Solovov*et al.*,*Two dimensional readout in a liquid xenon ionisation chamber*, Nucl. Instr. and Meth. A **477** (2002), pp.184-190.

[9] V.M. Atrazhev *et al.*, *Electron Transport Coefficients in Liquid xenon*, IEEE International Conference on Dielectric Liquids 2005, pp. 329-332.

[10] K.L. Giboni *et al.*, *Fast Timing Measurements of Gamma-ray Events in Liquid xenon*, IEEE Transactions on Nuclear Science, Vol. **52** (2005), No.5, pp. 1800-1804.

[11] V.N. Solovov *et al.*, *Study of Large Area Avalanche Photodiode for Detecting Liquid xenon Scintillation*, IEEE Transactions on Nuclear Science, Vol. **47** (2000), No.4, pp.1307-1310.

[12] D. Bryman *et al.*, *Reconstruction capabilities of a microPET detector based on Liquid Xenon technology*, in preparation.

[13] O. Bunemann, T.E. Cranshaw, J.A. Harvey, *Design of Grid Ionization Chambers*, Canadian Journal of Research, Vol. **27** (1949), Sec. A.

[14] Gas Purifiers and Particle Filters, NuPure Corporation, Ottawa ON K2S 1E7 Canada

[15] J.P. Martin, P.A. Amaudruz, *A 48 Channel Pulse Shape Digitizer with DSP*, IEEE Transactions on Nuclear Science, Vol. **53** (2006), No.3.

[16] Large Area Avalanche Photodiodes (LAAPDs), Advanced Photonics Inc., Camarillo, CA.

[17] T. Doke *et al.*, *Absolute Scintillation Yields in Liquid Argon and Xenon for Various Particles*, Jpn. J. Appl. Phys., Vol **41** (2002), pp. 1538-1545.

[18] E. Conti for the EXO Collaboration, *Correlated Fluctuations between Luminescence and Ionization in Liquid xenon*, Phys. Rev. B **68** (2003), 054201.

[19] L.S. Miller, S. Howe, W.E. Spear, *Charge Transport in Solid and Liquid Ar, Kr, and Xe*, Phys. Rev., Vol. **166** No. 3, (1968), 871

[20] H.J. Crawford *et al.*, *Ionization And Scintillation Signals Produced By Relativistic La Ions In Liquid Argon*, Nucl. Instrum. Meth. A **256** (1987), 47.

[21] K. Ni *et al.*, *Performance of a Large Area Avalanche Photodiode in a Liquid xenon Ionization and Scintillation Chamber*, Nucl. Instr. and Meth. A, **551** (2005) 356.

[22] J.L. Rodgers, W.A. Nicewander, *Thirteen Ways to Look at the Correlation Coefficient*, The American Statistician, Vol. **42** (1988), pp. 59-66.

[23] E. Shibamura *et al.*, *Test of the Recombination Model for the Energy Resolution in an Ionization Chamber Filled with Liquid Argon or Xenon*, Jpn. J. Appl. Phys., Vol **34** (1995), pp. 1897-1900.

[24] S. Agostinelli *et al.* [GEANT4 Collaboration], *GEANT4: A simulation toolkit*, Nucl. Instrum. Meth. A **506** (2003), 250.